Correlated electronic structure of colossal thermopower $FeSb_2$: An ARPES and *ab initio* study

A. Chikina,[1,2,*] J.-Z. Ma,[1,*] W. H. Brito,[3,4,*] S. Choi,[5] P. Sémon,[5] A. Kutepov,[5] Q. Du,[5,6] J. Jandke,[1] H. Liu,[1] N. C. Plumb,[1] M. Shi,[1] C. Petrovic,[5,6] M. Radovic,[1,†] and G. Kotliar[5,4]

[1]*Swiss Light Source, Paul Scherrer Institut, CH-5232 Villigen, Switzerland*

[2]*Department of Physics and Astronomy, Interdisciplinary Nanoscience Center, Aarhus University, 8000 Aarhus C, Denmark*

[3]*Departamento de Física, Universidade Federal de Minas Gerais, C. P. 702, 30123-970 Belo Horizonte, Minas Gerais, Brazil*

[4]*Department of Physics and Astronomy, Rutgers, the State University of New Jersey, Piscataway, New Jersey 08854, USA*

[5]*Condensed Matter Physics and Materials Science Department, Brookhaven National Laboratory, Upton, New York 11973, USA*

[6]*School of Materials Science and Engineering, Stony Brook University, Stony Brook, New York 11790, USA*

(Received 5 March 2020; accepted 27 April 2020; published 19 May 2020)

Iron antimonide ($FeSb_2$) with peculiar colossal thermopower of about -45 mV/K at 10 K is a mysterious material, and a unified microscopic description of this phenomenon is far from being achieved. Combining angle-resolved photoemission spectroscopy (ARPES) and *ab initio* calculations, we find that the intricate electronic structure of $FeSb_2$ consists of two bands near the Fermi energy: the weakly dispersing strongly renormalized α band and the holelike β band that intersect at Γ and Y points of the Brillouin zone. In addition, we found the surface state originated from the bulk β band. While both bulk bands upshift towards the Fermi level upon raising of the temperature, the weakly dispersing surface states vanish above 100 K. The structural distortions and/or a mixture of the localized low-spin state with the delocalized high-spin state populated with temperature could be responsible for this temperature dependence. Our study reveals that the sizable renormalization of the nondispersing α band and the hybridization with the holelike β band cause the local increase of the density of states, consequently raising the colossal thermopower in $FeSb_2$.

DOI: 10.1103/PhysRevResearch.2.023190

I. INTRODUCTION

Thermoelectricity in correlated electron materials is of great practical importance as they can exhibit giant thermopower values at low temperatures [1–4]. This is well exemplified by iron antimonide ($FeSb_2$), which hosts a colossal thermopower varying from about 1–2 to 45 mV/K [5–7]. The orthorhombic $FeSb_2$ [Fig. 1(a)] appears to be a narrow-gap semiconductor that exhibits insulator-to-metal transitions [8,9], unusual magnetic properties [10], and enhanced quasiparticle masses upon chemical substitution [11]. However, its colossal thermopower is far above the Mott value of the order of $k_B/e = 0.08$ mV/K, which is expected and usually recorded in metals or semiconductors [4,12].

It has been proposed that the colossal thermopower of $FeSb_2$ has an electronic origin due to electronic correlations associated with the Fe $3d$ states [5,13]. However, to date, there is no quantitative theory which incorporates the strong electronic correlations of the Fe $3d$ electrons and reproduces the value of $FeSb_2$ colossal thermopower. Furthermore, the energy gap Δ required to explain the experimental thermopower stemming from multiband electronic correlations in the absence of the phonon-mediated vertex corrections is about 450 meV [4], which is too large compared to experimental values of Δ between 30 and 70 meV [8,14,15]. More recently, phonon-drag mechanisms associated with defect-induced in-gap states have been proposed as the origin of the anomalous thermopower [16]. Within this picture, the thermopower enhancement up to about 16 mV/K was explained [6,16].

The model which describes band structure that gives a higher figure of merit zT was addressed by Mahan and Sofo [17], and later, it was successfully used to boost the thermopower of PbTe-based materials [18]. According to the Mahan-Sofo concept [17], a sharp peak in the density of states near the Fermi level can give rise to large thermopowers. This kind of feature can be found in the spectra of Kondo insulators or iron-based compounds where the electron-electron correlations can give rise to narrow bands [19]. In order to elucidate the low-energy excitation spectrum of $FeSb_2$, we disclose the electronic structure of $FeSb_2$ using a combination of angle-resolved photoemission spectroscopy (ARPES) and many-body first-principles calculations. More importantly, we demonstrate the existence of considerable electronic correlations of the Fe $3d$ states as well as intrinsic features in $FeSb_2$ electronic structure which are beneficial for large thermoelectric responses.

II. RESULTS AND DISCUSSIONS

Figure 1(d) presents the constant energy cut as a function of photon energy near 0.4 eV binding energy (BE) along the k_y crystallographic direction. The corresponding cuts

*These authors contributed equally to this work.
†Corresponding author: milan.radovic@psi.ch

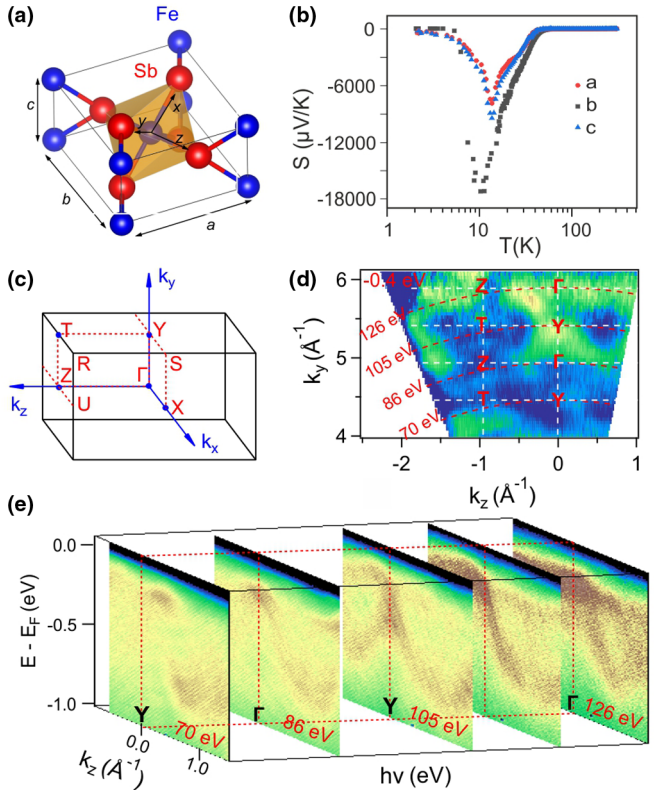

FIG. 1. (a) Crystal structure of $FeSb_2$ (space group *Pnnm*). The unit-cell dimensions are $a = 5.83$ Å, $b = 6.51$ Å, and $c = 3.16$ Å. The octahedron formed by the Fe (blue) and the six Sb (red) neighbor atoms is illustrated in orange. (b) Seebeck coefficient S as a function of temperature T for the thermal gradient along axes in zero magnetic field. (c) Sketch of the $FeSb_2$ Brillouin zone. (d) Isoenergy surface taken along k_y at 0.4 eV BE. (e) Two-dimensional ARPES cuts obtained at several photon energies along the Γ-Z direction.

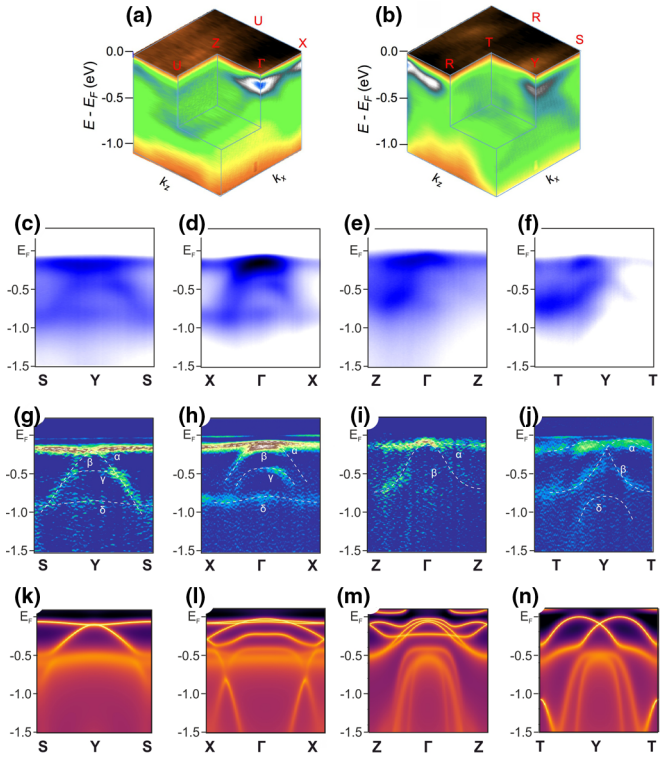

FIG. 2. (a) and (b) Full ARPES 3D mapping. (c)–(f) ARPES spectra at different high-symmetric directions in the BZ. (g)–(j) The spectra visualized using the curvature methods. The α band is still visible in (f) and (j) due to the k_y broadening. (k)–(n) LQSGW+DMFT calculated spectral functions at 50 K along the same high-symmetry directions as ARPES data.

along high-symmetry directions [Fig. 1(c)] taken at different photon energies are presented in Fig. 1(e). Indeed, some experimental reports [20,21] showed ARPES spectra of $FeSb_2$ but required only along one direction. Figures 2(a) and 2(b) and 2(c)–2(f) display the detailed experimental ARPES three-dimensional (3D) mapping in k space and cuts along the high-symmetry directions, respectively. Further, using the curvature method [22], the bands are enhanced [Figs. 2(g)–2(j)] and compared with the calculations. The experimentally obtained band structure of $FeSb_2$ is composed of two bands near the Fermi energy E_F: a light, dispersive holelike band (called here the β band) and a heavy, almost flat band [called the α band; Figs. 2(g)–2(j)]. Neither crosses E_F at low temperatures, and consequently, a gap below 100 meV is formed. These two bands intersect at the Γ point in the ΓXUZ plane and near the Y point in the $YSRT$ plane. The third holelike γ band emerges at Γ and Y points [Fig. 2(g)] around 0.5 eV and has weak dispersion along the k_y direction. This γ band intersects with the other weakly dispersing δ band at ∼0.8 eV of BE. While the α band is weakly dispersive in all directions (along which ARPES cuts are taken), the β band shows strong anisotropy, which can be quantified by the effective mass m^* for every measured direction: $m_x^* = 1.1m_e$–$4.3m_e$ (m_e is the free-electron mass) along the a axis, $m_z^* = 1.4m_e$–$3.6m_e$ along the c axis, and $m_y^* = 10m_e$–$11m_e$ along the b axis. The observed anisotropy in the band structure of $FeSb_2$ agrees well with anisotropy in the transport data [Fig. 1(b)].

In order to fully understand $FeSb_2$ electronic structure and underlying physics, ARPES data were compared with band structures obtained within density-functional theory (DFT), linearized quasiparticle self-consistent *GW* (LQSGW) methods, and LQSGW + dynamical mean-field theory (DMFT)-based spectral functions evaluated at 50 K (see Appendix A). As shown in Fig. 6 (see Appendix B), the band structures obtained within DFT methods do not agree with our experimental data, where the DFT [local-density approximation (LDA)] fails to capture the semiconducting nature of $FeSb_2$. LDA+DMFT calculations also cannot foresee the semiconducting phase of $FeSb_2$ at low temperatures. Indeed, the LQSGW predicts that $FeSb_2$ is a semiconductor, but with an overestimated band gap in comparison with the experiments.

Employment of the LQSGW+DMFT calculations where the electronic correlations beyond a many-body perturbation theory allowed reaching better agreement with the experimental band structure (Fig. 2). Indeed, our LQSGW+DMFT calculations predict sizable electron-electron correlations among the Fe $3d$ states of $FeSb_2$, with a quasiparticle weight $Z_{\mathrm{DMFT}} \sim 0.5$, which cannot be captured within the LQSGW method. The electronic correlations give rise to

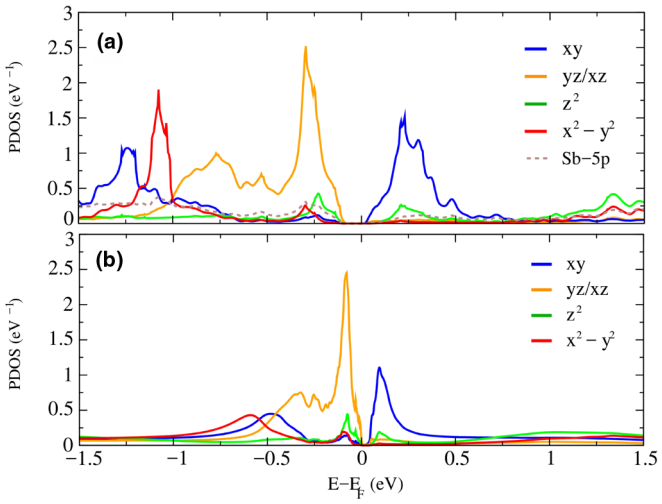

FIG. 3. (a) LQSGW- and (b) LQSGW+DMFT-based projected densities of states. The projections to Fe $3d_{xy}$, Fe $3d_{yz}/d_{xz}$, Fe $3d_{z^2}$, and Fe $3d_{x^2-y^2}$ are shown in blue, orange, green, and red. In (a) the projection to Sb $5p$ states is shown as a dashed brown line. These projected densities of states were obtained using the local axis shown in Fig. 1(a).

unambiguous renormalizations in the low-energy spectrum of $FeSb_2$. Besides the gap of around 70 meV, the low-energy part of the LQSGW+DMFT spectral functions shows the presence of a weakly dispersive α band and a more dispersive β band near E_F. Our LQSGW+DMFT calculations also suggest that these bands hybridize near the Γ and Y points [Figs. 2(k) and 2(l)]. Furthermore, the calculation finds a more dispersive behavior of the α band along the Y-T direction in comparison with the almost flat behavior of the same band along S-Y and Γ-X, which is in good agreement with the experiment [Figs. 2(g)–2(j)]. Thus, both ARPES data and calculated spectral functions indicate a low-dimensional behavior of the electronic structure of $FeSb_2$. Indeed, the corresponding anisotropy was recently found in optical conductivity measurements of $FeSb_2$ single crystals [15], which is in good agreement with one-dimensional semiconducting behavior of the optical properties along the b axis of the $Pnnm$ unit cell.

As pointed out by early investigations [23,24], low-dimensional behavior favors the appearance of high thermopower. Further, there is a high degeneracy of the low-energy bands along the Γ-X direction, as can be seen in Fig. 2(l). The orbital character of each band is shown in Fig. 3. As can be noticed, the top of the valence band is mainly due to Fe $3d_{yz}/d_{xz}$ states, while the bottom of the conduction band is mainly composed of Fe $3d_{xy}$ states. These findings indicate that the valence band in $FeSb_2$ exhibits an orbital degeneracy, which in turn is beneficial for large thermopowers since it increases the entropy per carrier. It is worth mentioning that this key feature was used successfully to enhance the thermopower of $PbTe_{1-x}Se_x$ to zT values up to 1.8 [25].

Moreover, the α band gives rise to a sharp peak near E_F which is of great importance to large thermopowers according

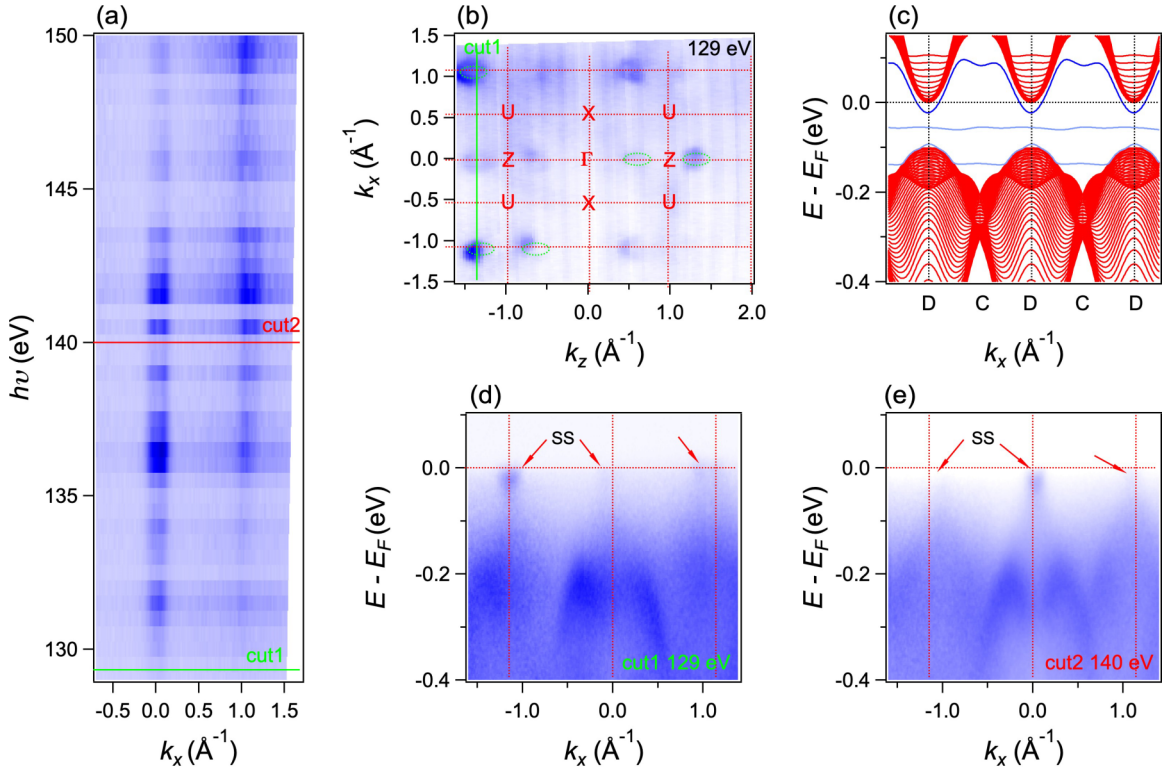

FIG. 4. (a) The raw isoenergy surface taken along k_y at the Fermi level. (b) Isoenergy cut (129 eV) on the (k_x, k_y) plane corresponding to cut 1 shown in (a). (c) Slab band structure calculated within the tight-binding approximation parametrized from our LQSGW calculations for a compressed $FeSb_2$ structure (see Appendix C). The surface bands are shown in blue, whereas the bulk bands are shown in red. (d) and (e) ARPES spectra along X-Γ-X taken at cuts 1 and 2, where SS denotes surface states.

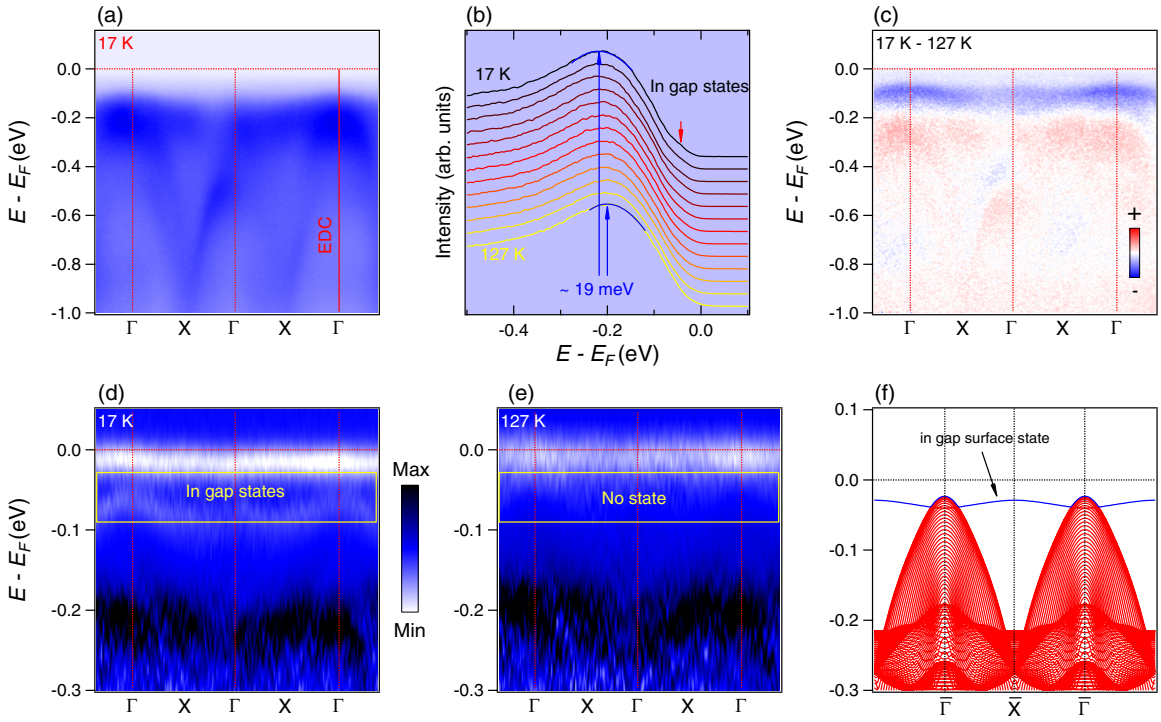

FIG. 5. (a) Electronic band structure along the Γ-X direction recorded at 17 K. (b) Temperature-dependent EDCs at the Γ point. The blue arrows show that the peak position shifts up around 19 meV upon heating from 17 to 127 K. (c) The photoemission intensity subtraction between the spectrum along the Γ-X direction obtained at 17 K [see (a)] and 127 K (not shown here). The "negative" blue flat pattern around −0.1 eV and the "positive" red flat pattern around −0.3 eV indicate that the band located at around −0.2 eV shifts up at all the momentum points along the Γ-X direction. (d) Curvature intensity plot of the data in (a). The yellow box marks the weakly dispersing surface-state-induced peak in the curvature intensity plot. (e) Same as (d), but recorded at 127 K. The weakly dispersing surface state disappear. (f) Slab calculation of the band structure along the projection of the Γ-X direction on the (010) surface. The blue curve indicates a nondispersive surface state near the Fermi level.

to the Mahan-Sofo theory [17]. Another essential finding is that the weakly dispersing α band is more gaped at the Y point than at the Γ point. This could be due to the fact that the holelike β band approaches the Fermi energy at the Γ point, which consequently brings up the α band, as seen in Figs. 2(h) and 2(i). As we show in Figs. 2(a) and 2(b), the valence-band maximum occurs at the Γ point, in contrast to band structures calculated using LQSGW, where the top of the valence band is located at the R point [see Appendix D, Figs. 11(a) and (b)]. Yet the calculated spectrum using the LQSGW+DMFT method in turn agrees with our experimental findings at this point, as shown in Figs. 11(c) and 11(d). Hence, the calculations outlined in this work demonstrate that a proper theoretical description of the electronic structure of $FeSb_2$ requires treatment beyond a perturbative approximation.

Although we observe the valence-band maximum at ∼0.1 eV BE, the sample surprisingly showed no charging effect during ARPES experiments at low temperature. This evidence suggests the presence of some states crossing the Fermi level. By acquiring more ARPES data at many different directions in k space we found a band at the ac plain is likely responsible for the robust surface conductivity. Figure 4(a) shows k_y dispersion at the Fermi energy proving the two-dimensional (2D) character of the observed band. Cuts taken at 129- and 140-eV photon energy [Figs. 4(b), 4(d), and 4(e)] clearly show the associated electronlike pocket at E_F.

To disentangle the origin of the 2D states observed by ARPES we have performed tight-binding calculations for a $FeSb_2$ slab terminated by Fe atoms. Our tight-binding calculations were parametrized from additional LQSGW calculations where the orthorhombic unit cell was slightly distorted to simulate a structural alteration. In particular, the b axis was compressed by 0.20 Å, while the a and c axes were elongated by 0.18 and 0.09 Å, respectively. The calculated band structure [Fig. 4(c)] reveals the presence of surface states (blue) within the LQSGW band gap. The electron pocket derived from this band along D-C cut ($k_z = 0.35$) parallel to Γ-X direction agrees well with experimental data, which points out the existence of a pocket along the D-C direction, as can be seen in Fig. 4(b). According to our DFT calculations for the $FeSb_2$ slab, this surface state is mainly formed by Fe 3d states (at the surface), while the Sb 5p states give a minor contribution to this band (see Fig. 9). The slab calculation of the band structure along the projection of the Γ-X direction on the (010) surface is depicted in Fig. 5(f). Our tight-binding calculations performed on both the bulk lattice parameters and the slab distorted by about 3% (see Fig. 10) suggest that these states [the blue line in Fig. 5(f)] might be a surface state which appears due to some weak structural distortion.

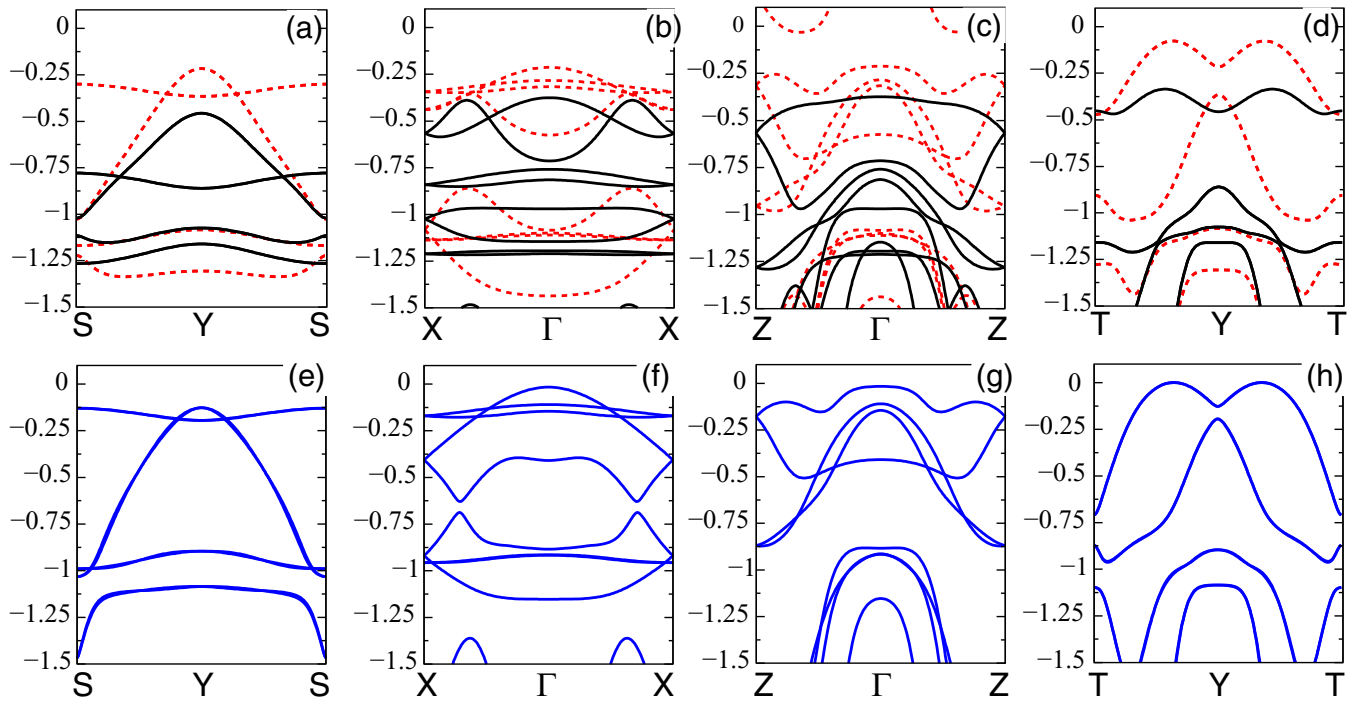

FIG. 6. (a)–(d) DFT band structures within the LDA (dashed red lines) and LDA-mBJ exchange-correlation potential (solid black lines). (e)–(h) The LQSGW band structures (blue lines).

To have a greater understanding of $FeSb_2$ thermopower we calculate the temperature dependence of its electronic structure near the Fermi level. For this experiment, we focused on the Γ-X direction where the light holelike (β band) and heavy (α band) bands are both clearly visible [Fig. 5(a)]. Figure 5(b) shows the energy distribution curves taken at cuts crossing the valence bands at the Γ point, whereas the curvature plots of the same cut at low (17 K) and higher (127 K) temperatures are presented in Figs. 5(d) and 5(e), respectively. Importantly, this data analysis reveals the presence of the weakly dispersing surface states around −60 meV. This surface state is sensitive to temperature ramping, becomes fainter at higher temperatures, and finally disappears around 100 K. In addition, the bulk bands shift toward the Fermi level upon heating up [Fig. 5(c)], as expected for an n-type semiconductor [26].

It was reported that temperature-dependent variation of the multiplet structure is reminiscent of the anisotropic diamagnetic to paramagnetic crossover [8]. The comparison of our calculation with ARPES data showed the high occupation of Fe states and its strong orbital degeneracy. In the octahedral crystal field Fe $3d$ orbitals split into higher e_g ($d_{x^2-y^2}/d_{z^2}$) orbitals and lower t_{2g} (d_{xy}, d_{xz}, and d_{yz}) orbitals, suggesting that the diamagnetic low-spin ground state is $t_{2g}^6 e_g^0$. All of these findings that the observed band shift might also be due to the thermal population of the excited high-spin ($t_{2g}^4 e_g^2$) state. On the other hand, our tight-binding calculations for the $FeSb_2$ slab indicate that this shift can also be caused by a structural distortion. The comparison between calculated band structures of nondistorted and distorted lattices (see Fig. 10) shows that the dispersion and the position of the holelike β band are very sensitive to the lattice parameters. In particular, we observe an enhancement of the splitting between α and holelike β bands, where the latter upshifts towards the Fermi energy upon lattice distortion. The β band also becomes less dispersive, and its hybridization with the α band is affected by the structural distortion [see Figs. 10(a) and 10(c)]. According to [18]

$$S = \frac{\pi^2 k_B^2 T}{3q}\left[\frac{1}{n}\frac{dn(E)}{dE} + \frac{1}{\mu}\frac{d\mu(E)}{dE}\right]_{E=E_F}, \qquad (1)$$

the Seebeck coefficient can be enhanced by a local increase of the density of states $n(E)$ near Fermi energy and by the change in the chemical potential as well. In Eq. (1), μ stands for the mobility, q stands for the carrier charge, and T stands for temperature. Indeed, the overlapping of the holelike dispersive β band and heavy α band gives rise to a local increase of the density of states in $FeSb_2$. In addition, the shift we observed of the β band near the Fermi energy for a distorted lattice that causes the increase of the density of states close to the Fermi energy can boost the thermopower further. The second term in Eq. (1) shows that further enhancement of the Seebeck coefficient in $FeSb_2$ can be achieved by defect engineering and impurity-level formation.

III. SUMMARY

In summary, we performed a detailed experimental and theoretical investigation of the $FeSb_2$ electronic structure. Obtained ARPES data revealed that the electronic structure of $FeSb_2$ near the Fermi energy consists of two bands: the strongly renormalized and weakly dispersing α band and the holelike β band. Our LQSGW+DMFT calculations reproduced well the experimentally depicted electronic structure,

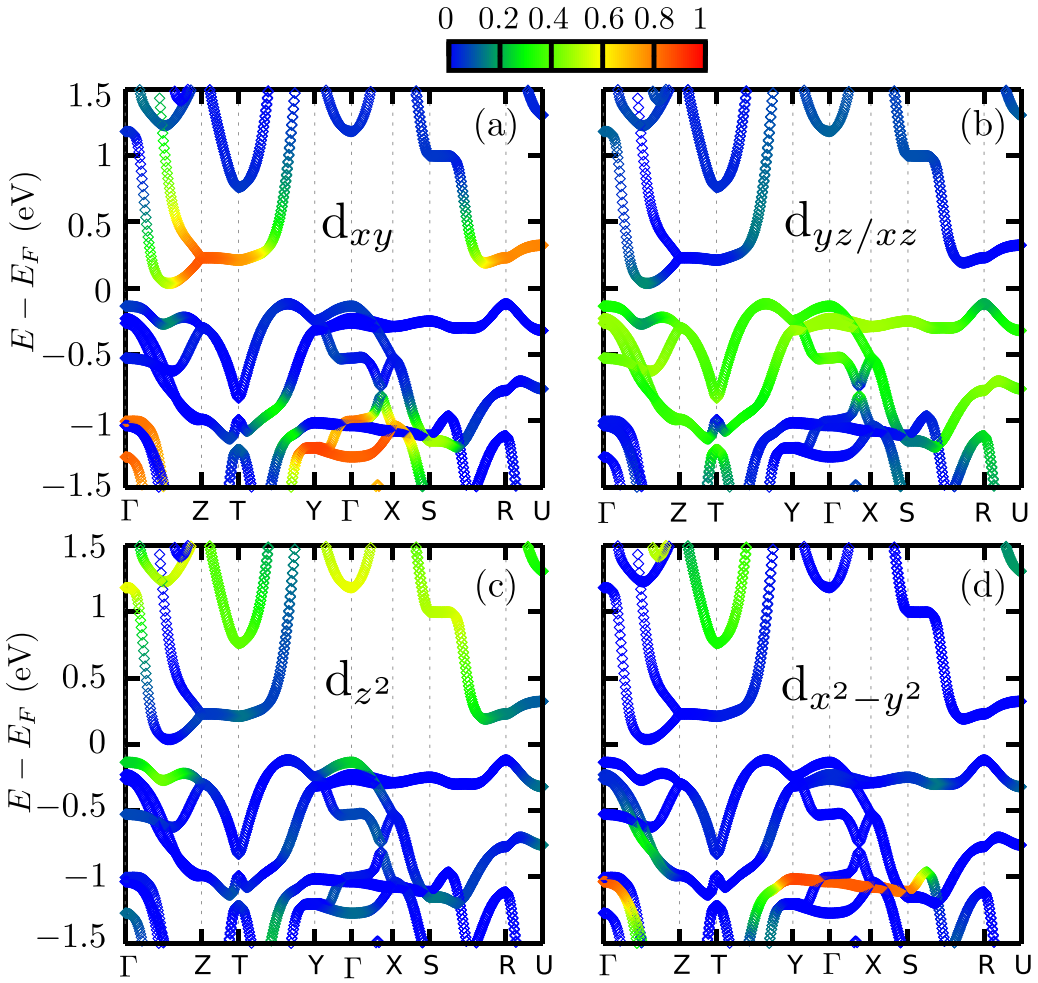

FIG. 7. Fe 3*d* orbital-resolved LQSGW band structure of $FeSb_2$. We present the contributions to the iron d_{xy}, d_{yz}/d_{xz}, d_{z^2}, and $d_{x^2-y^2}$ orbitals in (a), (b), (c), and (d), respectively.

providing clear evidence of sizable electronic correlations ($Z_{\mathrm{DMFT}} \sim 0.5$) which causes band renormalization of the Fe 3*d* states in the low-energy region. However, the modest value of renormalization and the distinct orbital character of valence and conduction bands exclude the Kondo picture of $FeSb_2$. The temperature dependency of weakly dispersing states near the Fermi level indicates a change in the degree of electron localization related to electron correlation effects. Based on our study, the enhancement of the thermoelectric figure of merit of $FeSb_2$ can be obtained by band engineering, making the α band further renormalized and β band more dispersing.

ACKNOWLEDGMENTS

This work was supported by the U.S. Department of Energy, Office of Science, Basic Energy Sciences as a part of the Computational Materials Science Program. This research used resources of the National Energy Research Scientific Computing Center (NERSC), a U.S. Department of Energy Office of Science User Facility operated under Contract No. DE-AC02-05CH11231. M.R. and J.-Z.M. were supported by Project No. 200021_182695 funded by the Swiss National Science Foundation. ARPES experiments were conducted at the Surface/Interface Spectroscopy (SIS) beamline of the Swiss Light Source at the Paul Scherrer Institut in Villigen, Switzerland. The authors thank the technical staff at the SIS beamline for their support. A.C. acknowledges VILLUM FONDEN through the Center of Excellence for Dirac Materials (Grant No. 11744).

APPENDIX A: FIRST-PRINCIPLES METHODS

1. $FeSb_2$ bulk

Our DFT calculations were performed within the local-density approximation (LDA) [27] and modified Becke-Johnson (LDA-mBJ) exchange-correlation potential [28], as implemented in WIEN2K [29]. The linearized quasiparticle self-consistent *GW* (LQSGW) calculations were performed using the FLAPWMBPT code [30–32] where the muffin-tin radii in the Bohr radius are 2.6 and 2.2 for Fe and Sb, respectively. In the calculation of polarizability and self-energy, unoccupied states with an energy up to 200 eV from the Fermi energy were taken into account. In our LQSGW+DMFT calculations performed within COMSUITE [33,34], projectors to the correlated Fe 3*d* orbitals were constructed using Fe 3*d*- and Sb 5*p*-based maximally localized Wannier functions [35]. These projectors span the electronic states in the energy window

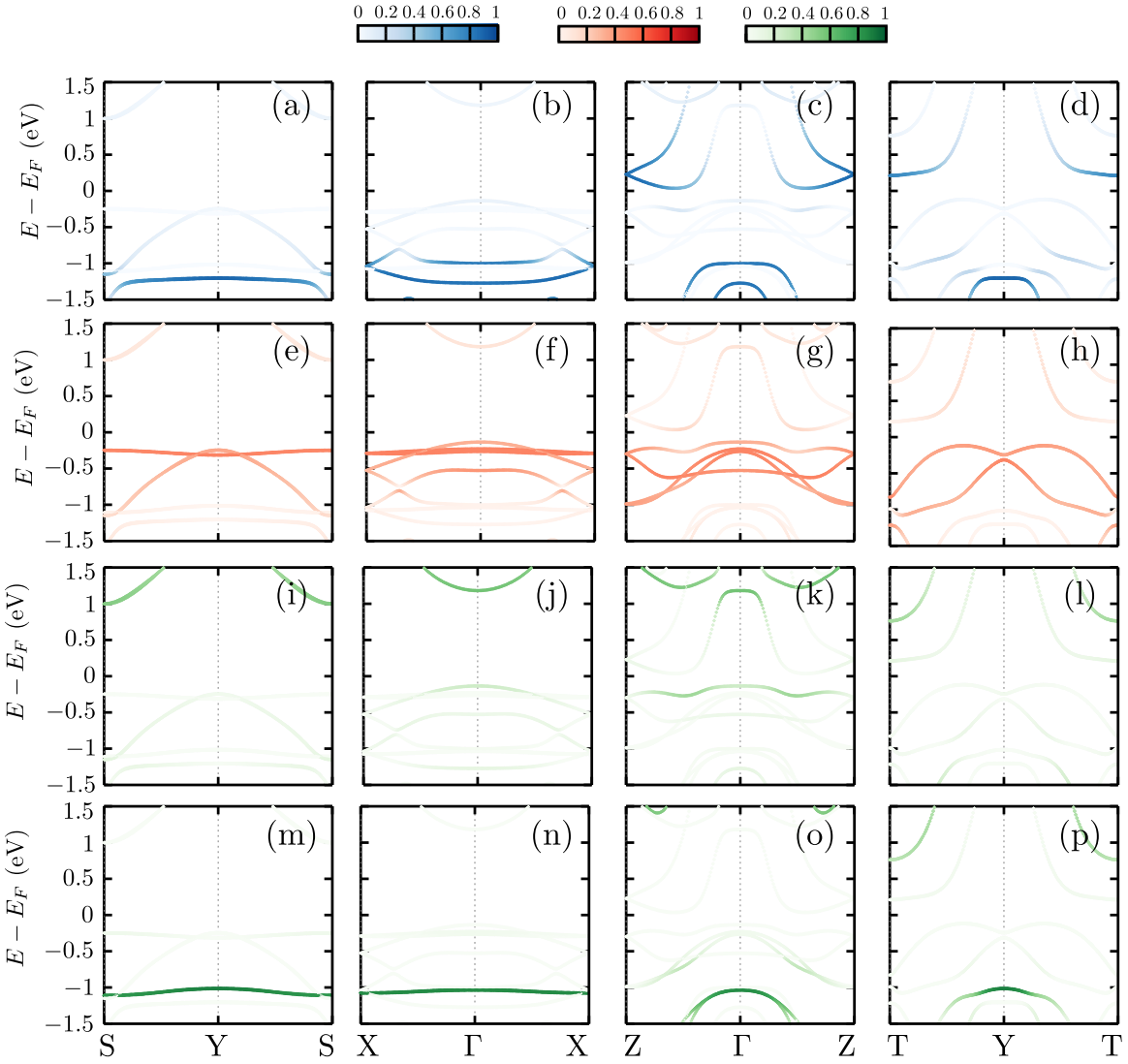

FIG. 8. Fe 3*d* orbital-resolved LQSGW band structure along the same high-symmetry directions in the BZ as in the ARPES data. Projections to (a)–(d) Fe d_{xy}, (e)–(h) Fe d_{yz}/d_{xz}, and (i)–(l) Fe d_{z^2} and (m)–(p) Fe $d_{x^2-y^2}$ are shown in blue, red, and green, respectively.

of $E_F \pm 8$ eV in a $15 \times 15 \times 30$ k grid. It is important to mention that by using this large energy window we construct very localized Fe 3*d* orbitals. Next, we evaluate the local self-energy associated with the Fe 3*d* orbitals within dynamical mean-field theory (DMFT) [36] using static U_d and J_H. These two quantities are evaluated by using a modification of the constrained random-phase approximation [33,37], which avoids the screening from the correlated as well as hybridized bands. In particular, by using Slater's integrals [38,39] we obtain $U_d = 4.8$ eV and $J_H = 1.0$ eV. Finally, we mention that the Feynman diagrams included in both LQSGW and DMFT (double counting) are the local Hartree and local *GW* diagrams. They are computed using the local projection of the LQSGW's Green's function and the local Coulomb matrix constructed by U_d and J_H.

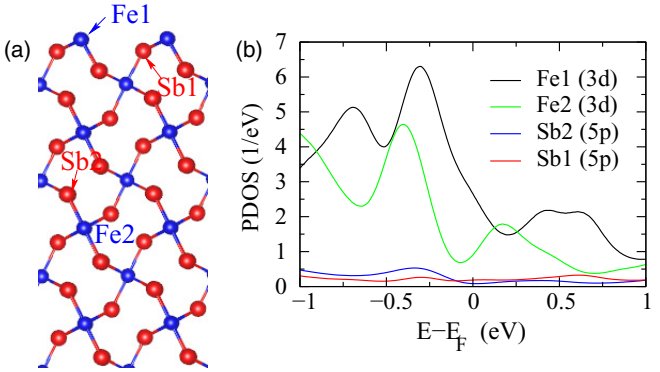

FIG. 9. (a) Theoretical slab model for the $FeSb_2$ surface which is terminated in Fe (blue spheres). (b) Projected density of states on the Fe1, Fe2, Sb1, and Sb2 sites illustrated in (a).

2. $FeSb_2$ surface

Our DFT calculations for the $FeSb_2$ surface were performed within the Perdew-Burke-Ernzerhof generalized gradient approximation [40] using the QUANTUM ESPRESSO suite [41]. In our calculations a plane-wave basis-set with an

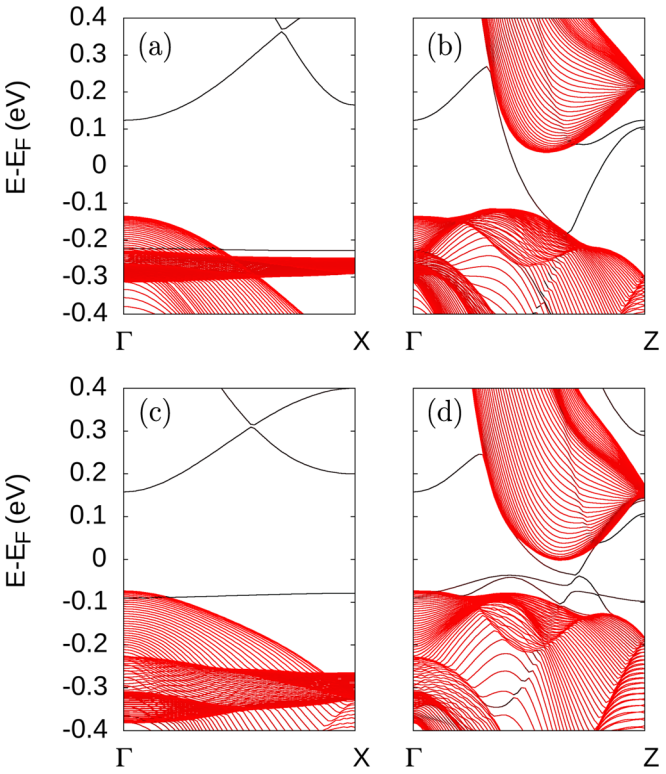

FIG. 10. Tight-binding band structures parametrized from our LQSGW calculations. In (a) and (b) we present the obtained band structures for the slab constructed using the bulk lattice parameters along Γ-X and Γ-Z, respectively. In (c) and (d) we show the band structures along the same directions for a distorted slab where the axes were modified by about 3% from their bulk values.

energy cutoff of 30 Ry was employed. The atomic positions were relaxed until the total forces on each atom were smaller than 10^{-3} a.u. Further, in our calculations the electron-ion interactions were described through ultrasoft pseudopotentials [42].

APPENDIX B: DFT AND LQSGW BAND STRUCTURES

Our calculated DFT (LDA), DFT (LDA-mBJ), and LQSGW band structures are shown in Fig. 6. Figure 6 displays the electronic band structures along the Y-S, Γ-X, Γ-Z, and Y-T high-symmetry directions of the Brillouin zone [see Fig. 1(c) in the main text].

First, our DFT (LDA) calculations fail to describe the semiconducting nature of $FeSb_2$. This can be overcome by using the mBJ exchange-correlation potential [28], which is better at describing the band gaps of semiconductors than LDA. For $FeSb_2$ the DFT (LDA-mBJ) method predicts an overestimated band gap of 0.20 eV. Further, one can notice that the occupied part of the band structures (bands below zero) [Figs. 6(a)–6(d)] calculated within DFT (LDA) agrees better with the ARPES data than the one obtained with DFT (LDA-mBJ). For instance, the DFT (LDA-mBJ) band structure along Y-S [Fig. 6(a)] shows a dispersing band near E_F and an almost flat band (reminiscent of α band) at -0.88 eV at the Y point, in disagreement with ARPES. Although the mBJ exchange-correlation potential allows the correct description

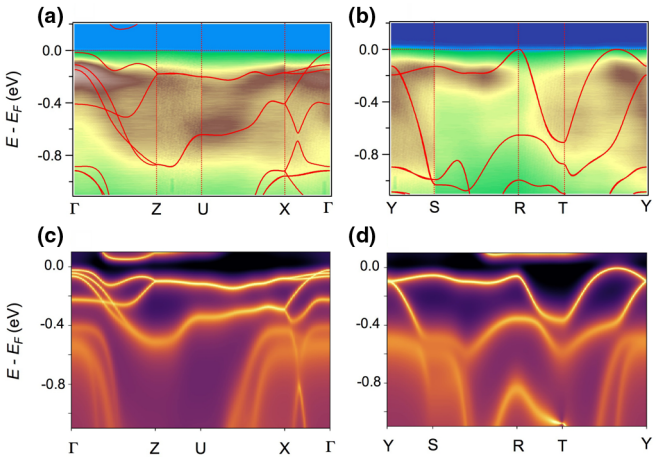

FIG. 11. ARPES-derived spectra together with calculated LQSGW band structure of $FeSb_2$ along (a) Γ-Z-U-X-Γ and (b) Y-S-R-T-Y. (c) and (d) The LQSGW + DMFT spectral functions at 50 K along the same directions.

of the insulating nature of $FeSb_2$, the electronic correlations taken into account within the mBJ approximation cannot describe the experimental electronic structure of $FeSb_2$.

Within the LQSGW approximation [31,32] we find that $FeSb_2$ has a gap of ∼160 meV with the occupied part of the spectrum in better agreement with the ARPES data, even though, the corresponding α and β bands do not cross exactly at the Γ and Y points [Figs. 1(e)–1(h)]. Also, the LQSGW calculation predicts additional bands around -0.5 and -1 eV (at the Γ point) which are reminiscent of the γ and δ bands observed in ARPES, as can be seen in Figs. 2(g) and 2(h) in the main text. The orbital-resolved LQSGW band structure is shown in Figs. 7 and 8. From these figures one can observe that the valence band is mainly composed of Fe d_{yz}/d_{xz} states, whereas the conduction band is mainly of Fe d_{xy} character. The band around -1.25 eV observed in the band structure calculated by the LQSGW [Figs. 6(e) and 6(f)] is due to Fe $3d_{xy}$ states, indicating that this band is bonding-state-like while the conduction states are antibondinglike. In addition, the band around -1 eV is mainly from the Fe $3d_{x^2-y^2}$ states. Finally, it is noteworthy that the Sb $5p$ states make a minor contribution to the bands around the Fermi energy.

APPENDIX C: DFT AND TIGHT-BINDING CALCULATIONS FOR THE $FeSb_2$ SURFACE

In our investigation of the $FeSb_2$ surface we initially employed DFT calculations to relax the atomic positions of a slab generated through a ac-cleavage plane. In Fig. 9(a) we illustrate the resulting iron-terminated surface. According to our calculations, the metallic surface states are mainly due to the Fe $3d$ states of the Fe1 site, as shown in the projected density of states in Fig. 9(b).

Further, we performed tight-binding calculations, parametrized from our LQSGW calculations, for a slab with 30 layers. In particular, we considered two distinct slabs, one constructed using the bulk lattice parameters and another with a distorted structure, where we compressed the b axis and elongated the a and c axes by about 3% from their bulk

values. With the distorted slab structure we intend to simulate any possible surface relaxation which might occur in our samples. In Figs. 10(a) and 10(b) we present the evaluated band structure along the Γ-X and Γ-Z directions for the slab constructed using the bulk lattice parameters. As can be noticed, there is no electron pocket along Γ-X or between Γ and Z. On the other hand, the band structure of the distorted slab [Fig. 10(d)] does show a small electron pocket between Γ and Z, in better agreement with our experimental data [see Fig. 4(b) in the main text].

APPENDIX D: LQSGW+DMFT SPECTRAL FUNCTION

As discussed in the main text our ARPES data indicate the maximum of the valence band takes place at the Γ point. As shown in Figs. 11(a) and 11(b) our LQSGW band structure predicts that the maximum takes place at the R point, in contrast to our ARPES data. On the other hand, one can observe that the calculated LQSGW+DMFT spectral functions predict the valence-band maximum at the Γ point [Figs. 11(c) and 11(d)], in better agreement with our experimental findings.

[1] J. M. Tomczak, K. Haule, and G. Kotliar, Proc. Natl. Acad. Sci. USA **109**, 3243 (2012).
[2] G. Pálsson and G. Kotliar, Phys. Rev. Lett. **80**, 4775 (1998).
[3] W. Koshibae and S. Maekawa, Phys. Rev. Lett. **87**, 236603 (2001).
[4] J. M. Tomczak, K. Haule, T. Miyake, A. Georges, and G. Kotliar, Phys. Rev. B **82**, 085104 (2010).
[5] A. Bentien, S. Johnsen, G. K. H. Madsen, B. B. Iversen, and F. Steglich, Europhys. Lett. **80**, 17008 (2007).
[6] H. Takahashi, R. Okazaki, S. Ishiwata, H. Taniguchi, A. Okutani, M. Hagiwara, and I. Terasaki, Nat. Commun. **7**, 12732 (2016).
[7] Q. Jie, R. Hu, E. Bozin, A. Llobet, I. Zaliznyak, C. Petrovic, and Q. Li, Phys. Rev. B **86**, 115121 (2012).
[8] C. Petrovic, J. W. Kim, S. L. Bud'ko, A. I. Goldman, P. C. Canfield, W. Choe, and G. J. Miller, Phys. Rev. B **67**, 155205 (2003).
[9] A. Perucchi, L. Degiorgi, R. Hu, C. Petrovic, and V. F. Mitrović, Eur. Phys. J. B **54**, 175 (2006).
[10] C. Petrovic, Y. Lee, T. Vogt, N. D. Lazarov, S. L. Bud'ko, and P. C. Canfield, Phys. Rev. B **72**, 045103 (2005).
[11] A. Bentien, G. K. H. Madsen, S. Johnsen, and B. B. Iversen, Phys. Rev. B **74**, 205105 (2006).
[12] M. Cutler and N. F. Mott, Phys. Rev. **181**, 1336 (1969).
[13] P. Sun, N. Oeschler, S. Johnsen, B. B. Iversen, and F. Steglich, Phys. Rev. B **79**, 153308 (2009).
[14] A. Herzog, M. Marutzky, J. Sichelschmidt, F. Steglich, S. Kimura, S. Johnsen, and B. B. Iversen, Phys. Rev. B **82**, 245205 (2010).
[15] C. C. Homes, Q. Du, C. Petrovic, W. H. Brito, S. Choi, and G. Kotliar, Sci. Rep. **8**, 11692 (2018).
[16] M. Battiato, J. M. Tomczak, Z. Zhong, and K. Held, Phys. Rev. Lett. **114**, 236603 (2015).
[17] G. D. Mahan and J. O. Sofo, Proc. Natl. Acad. Sci. USA **93**, 7436 (1996).
[18] J. P. Heremans, V. Jovovic, E. S. Toberer, A. Saramat, K. Kurosaki, A. Charoenphakdee, S. Yamanaka, and G. J. Snyder, Science **321**, 554 (2008).
[19] J. M. Tomczak, J. Phys.: Condens. Matter **30**, 183001 (2018).
[20] S. Imada, K. Terashima, A. Sekiyama, S. Suga, A. Yamasaki, K. Mima, Y. Miyata, R. Yamaguchi, Y. Tachimori, Y. Yamanoi *et al.*, UVSOR Activity Report No. 37, National Institutes of Natural Sciences in Japan (UVSOR, 2009), p. 106.
[21] S. Imada, K. Terashima, A. Yamasaki, K. Mima, Y. Miyata, R. Yamaguchi, Y. Tachimori, Y. Yamanoi, H. Eto, Y. Matsui *et al.*, UVSOR Activity Report No. 38, National Institutes of Natural Sciences in Japan (UVSOR, 2010), p. 94.
[22] P. Zhang, P. Richard, T. Qian, Y.-M. Xu, X. Dai, and H. Ding, Rev. Sci. Instrum. **82**, 043712 (2011).
[23] L. D. Hicks and M. S. Dresselhaus, Phys. Rev. B **47**, 16631 (1993).
[24] R. Kim, S. Datta, and M. S. Lundstrom, J. Appl. Phys. **105**, 034506 (2009).
[25] Y. Pei, X. Shi, A. LaLonde, H. Wang, L. Chen, and G. J. Snyder, Nature (London) **473**, 66 (2011).
[26] T. Takeuchi, Y. Toyama, and A. Yamamoto, Mater. Trans. **51**, 421 (2010).
[27] W. Kohn and L. J. Sham, Phys. Rev. **140**, A1133 (1965).
[28] F. Tran and P. Blaha, Phys. Rev. Lett. **102**, 226401 (2009).
[29] P. Blaha, K. Schwarz, G. K. H. Madsen, D. Kvasnicka, and J. Luitz, *An Augmented Plane Wave+ Local Orbitals Program for Calculating Crystal Properties*, edited by K. Schwarz (Technische Universitat Wien, Vienna, 2001).
[30] A. Kutepov, S. Y. Savrasov, and G. Kotliar, Phys. Rev. B **80**, 041103(R) (2009).
[31] A. Kutepov, K. Haule, S. Y. Savrasov, and G. Kotliar, Phys. Rev. B **85**, 155129 (2012).
[32] A. Kutepov, V. Oudovenko, and G. Kotliar, Comput. Phys. Commun. **219**, 407 (2017).
[33] S. Choi, A. Kutepov, K. Haule, M. van Schilfgaarde, and G. Kotliar, npj Quantum Mater. **1**, 16001 (2016).
[34] Center for Computational Material Spectroscopy and Design, COMSUITE, https://www.bnl.gov/comscope.
[35] N. Marzari, A. A. Mostofi, J. R. Yates, I. Souza, and D. Vanderbilt, Rev. Mod. Phys. **84**, 1419 (2012).
[36] A. Georges, G. Kotliar, W. Krauth, and M. J. Rozenberg, Rev. Mod. Phys. **68**, 13 (1996).
[37] F. Aryasetiawan, M. Imada, A. Georges, G. Kotliar, S. Biermann, and A. I. Lichtenstein, Phys. Rev. B **70**, 195104 (2004).
[38] D. van der Marel and G. A. Sawatzky, Phys. Rev. B **37**, 10674 (1988).
[39] A. Kutepov, K. Haule, S. Y. Savrasov, and G. Kotliar, Phys. Rev. B **82**, 045105 (2010).
[40] J. P. Perdew, K. Burke, and M. Ernzerhof, Phys. Rev. Lett. **77**, 3865 (1996).
[41] P. Giannozzi, S. Baroni, N. Bonini, M. Calandra, R. Car, C. Cavazzoni, D. Ceresoli, G. L. Chiarotti, M. Cococcioni, I. Dabo *et al.*, J. Phys.: Condens. Matter **21**, 395502 (2009).
[42] D. Vanderbilt, Phys. Rev. B **41**, 7892 (1990).